Title

Characterization of the THz absorption spectra of nematic liquid crystals via THz time-domain spectroscopy using mode-locked Yb-doped fiber laser

Authors

Choi, Hansol

Kim, Jisu

Ahn, Soyeon

et al.

Publication Date

2021-10-01

DOI

10.1016/j.yofte.2021.102685

Optical Fiber Technology 66 (2021) 102685

Contents lists available at ScienceDirect

Optical Fiber Technology

journal homepage: www.elsevier.com/locate/yofte

Regular Articles

Characterization of the THz absorption spectra of nematic liquid crystals via THz time-domain spectroscopy using mode-locked Yb-doped fiber laser

Hansol Choi [a,1], Jisu Kim [a,1], Soyeon Ahn [a], Sang Pil Han [b], Zhongping Chen [c], Min Yong Jeon [a,d,*]

[a] Department of Physics, Chungnam National University, 99 Daehak-ro Yuseong-gu, Daejeon 34134, Republic of Korea
[b] Photonic/Wireless Devices Research Division, Electronics and Telecommunications Research Institute, Daejeon 34129, Republic of Korea
[c] Beckman Laser Institute, UC Irvine, Irvine, CA 92612, USA
[d] Instituted of Quantum Systems (IQS), Chungnam National University, 99 Daehak-ro Yuseong-gu, Daejeon, 34134, Republic of Korea

ARTICLE INFO

Keywords:
Yb-doped fiber laser
Mode-locked fiber laser
Time-domain THz spectroscopy
Nematic liquid crystals

ABSTRACT

In this paper, the terahertz (THz) absorption spectra of a nematic liquid crystal (NLC) cell are estimated via THz time-domain spectroscopy (TDS) using a mode-locked Yb-doped fiber laser as the pump source. The THz-TDS system is implemented by using a dipole antenna as an emitter and a bow tie antenna as a receiver. A THz emission bandwidth exceeding 2.2 THz is achieved corresponding to a free spacing of 220 mm and a signal-to-noise ratio exceeding 30 dB. Subsequently, this system was utilized to measure and analyze the THz absorption spectrum of an E7 NLC cell by applying an electric field. The conclusions experimentally confirmed that the absorption of the specific THz frequency of the cell is inversely proportional to the intensity of the electric field applied to the NLC cell.

1. Introduction

Terahertz (THz) waves exhibit both the straightness of light as well as the transmittance of microwaves, enabling non-destructive testing. Therefore, they enjoy a very wide range of applications. E.g., in spectroscopy, imaging technology, security screening, and medicine [1–10]. Applications of THz technology can be broadly classified into spectroscopy, imaging, and wireless communication technologies [11–22]. Spectroscopy has been applied in various fields such as biology, medical diagnosis, food inspection, explosion inspection for security screening, drug inspection, inspection of art, and environmental pollution monitoring. On the other hand, imaging technology has been applied to time-of-flight imaging, magnetic resonance imaging, and optical coherence tomography [13,16–19]. Finally, wireless communication technology has been recently applied to wireless communication between personal wireless devices, related to 5G or Internet of Things, over short indoor distances [20–22]. THz -based communication is also expected to be utilized in traffic control, autonomous driving, and remote health monitoring services.

THz spectroscopy can be divided into time domain spectroscopy (TDS) [14–15,23] based on pulse emission and frequency domain spectroscopy (FDS) based on the beating of two continuous-wave (CW) lasers [24,25]. The THz-TDS method is most popular. In this method, a pulse generated using a femto-second laser is irradiated onto a semiconductor or a nonlinear crystal. The generation and detection of THz pulses using a photoconductive antenna (PCA) requires periodic changes of at most 1 ps in electrical or optical signals. The bulky titanium sapphire laser (Ti:sapphire laser) used to be the most common choice for the pump light source in most of THz-TDS. However, in recent years, it has been replaced by femtosecond fiber lasers, which are smaller and exhibit higher power [13–15,23]. Due to their smaller size compared to solid-state lasers, femtosecond fiber lasers enjoy much higher mobility. THz-TDS architectures constructed based on a combination of a femtosecond fiber laser and photoconductive antennas (PCAs) exhibits excellent optical-THz conversion efficiency, low space constraints, and low system manufacturing and maintenance costs. On the other hand, mode-locked fiber lasers used in THz-TDS was primarily implemented using an Er- or Yb-doped fiber (YDF) as a gain medium. In particular, a mode locked YDF laser exhibits excellent performance in terms of a broad gain spectrum, excellent stability, high quantum efficiency, and

* Corresponding author.
E-mail address: myjeon@cnu.ac.kr (M.Y. Jeon).
[1] These authors contributed equally to this work.

https://doi.org/10.1016/j.yofte.2021.102685
Received 3 July 2021; Received in revised form 5 August 2021; Accepted 6 September 2021
Available online 15 September 2021

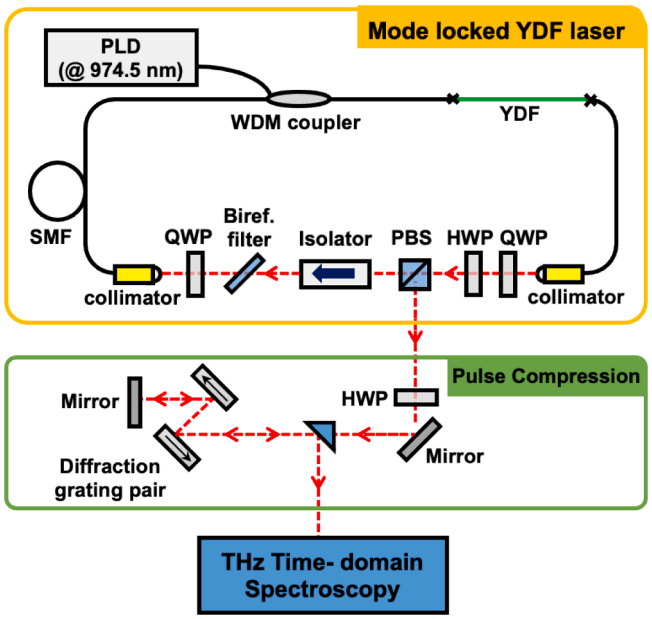

Fig. 1. Experimental setup for a mode-locked YDF laser and optical pulse compression (PLD: pump laser diode, WDM: wavelength division multiplexing, YDF: Yb-doped fiber, QWP: quarter wave-plate, HWP: half wave-plate, PBS: polarization beam splitter, Biref. filter: birefringent spectral filter).

compact size. Compared to a mode-locked Er-doped fiber laser, it can obtain a high output without using an optical amplifier, making it suitable as a THz pump source [15,26–28]. In rare-earth-doped fiber lasers, mode locking is implemented in various methods, such as nonlinear polarization rotation (NPR) [14–15,29–32], 2D material-based saturable absorbers [33–36], and non-linear loop mirrors [37] and others [38,39]. Among them, the Yb-doped fiber laser mainly uses the NPR method to implement mode locking.

On the other hand, liquid crystal (LC) devices have been studied for a long time because of their birefringence properties and have led to the development of many other optical devices that have contributed to the development of the electronics industry. The effective refractive index, absorption coefficient, and polarization of LC molecules with free molecular arrangement are dependent on the rotation of the directors when external stimuli, such as an electric field or temperature variation, are applied [40–44]. Although LCs are widely used and well characterized as optical devices, they have not been adequately explored in the THz range [45–49]. Proper utilization of such LC properties could lead to LC-based THz devices, such as LC-based THz switches, polarizers, and phase adjusters. Finally, extensive research on various THz devices, such as birefringent devices for millimeter waves, microwave delay lines, microwave phase delay gratings, and THz-Lyot filters, is ongoing [47–51].

In this paper, we demonstrate the implementation of PCA-based THz-TDS using a mode-locked YDF laser as a THz pump light source. A mode-locked fiber laser with YDF is employed as a gain medium to achieve mode-locking over the region comprising 1 μm center wavelength using a nonlinear polarization rotation (NPR) method [14,15,29–32], which serves the function of an artificial saturable absorber. As the femtosecond pulse is output directly from the oscillation of the mode-locked fiber laser in the normal dispersion region and exhibits a chirp owing to many frequency components, an oscillating pulse with a period of several ps is generated, resulting in the compression of the output pulse into a pulse with a period less than or equal to ~200 fs using a pair of diffraction gratings outside the resonator. Subsequently, a nematic liquid crystal (NLC) cell is fabricated and analyzed using THz-TDS. In particular, the dependence of the THz spectral characteristics of the NLC cell on the intensity of the applied electric field is measured and analyzed.

2. Experiments

A schematic diagram of the experimental setup for a mode locked YDF laser and a pulse compression system is depicted in Fig. 1 [29]. The box on the top denotes a mode locked YDF laser. It operates in normal dispersion mode and achieves passive mode-locking by employing the NPR method as a saturable absorber. It composes a laser diode with a center wavelength of 974.5 nm utilized as a pump light source, a 980/1030 nm wavelength division multiplexing (WDM) coupler, 25 cm-long YDF (Liekki®YB1200-4/125@nLIGHT) utilized as a gain medium, a 1.54 m-long single mode fiber (SMF), and two collimators within the optical fiber. In its capacity as a gain medium in this experiment, the YDF exhibits a 1200 dB/m peak absorption at 975 nm. The pump laser diode exhibits a maximum output power of 500 mW. The free space of 0.28 m length consists of a quarter wave plate (QWP), a half wave plate (HWP), an optical isolator, a birefringent spectral filter, and a polarization beam splitter (PBS). The birefringence spectral filter exhibits a center wavelength of 1030 nm and a bandwidth of 10 nm [29].

The pump light enters the resonator through the WDM coupler and the YDF emits light in the 1 μm band. When the emitted light enters the free space through the collimator, it passes through the QWP and the HWP and is divided into *s*-polarized light and *p*-polarized light in the PBS. The *s*-polarized component is used as the output and the *p*-polarized light proceeds to the SMF through the optical isolator, the birefringent wavelength filter, and the collimator through the QWP in the laser cavity. The total length of laser cavity is taken to be ~2.07 m, including the free space, and the pulse repetition rate is 103.75 MHz.

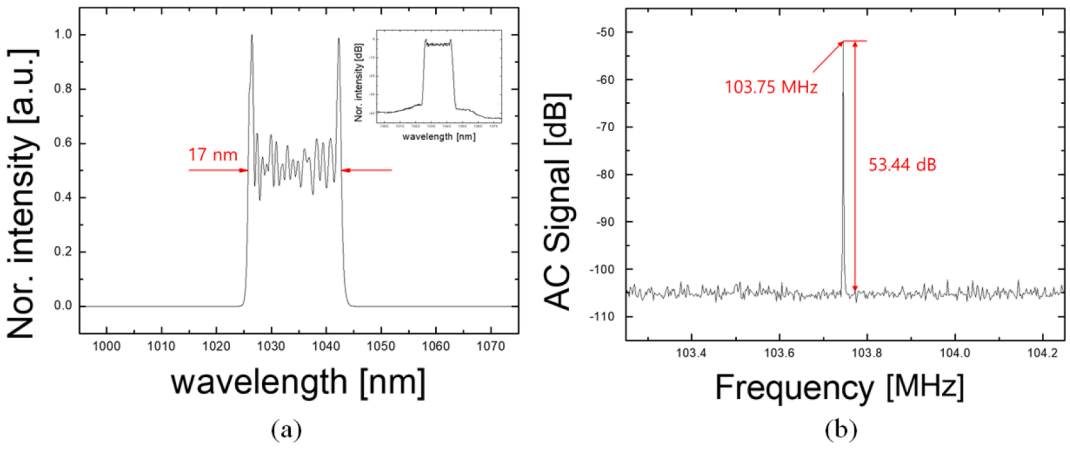

Fig. 2. (a) Optical spectrum and (b) RF-spectrum outputs of the mode-locked YDF laser.

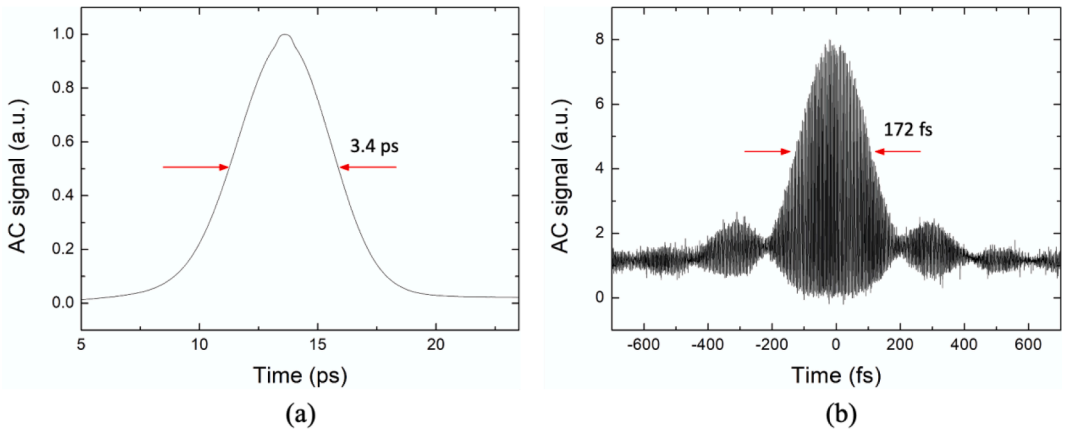

Fig. 3. (a) Autocorrelation trace of the pulse directly emitted from the mode locked YDF laser and (b) Autocorrelation trace of the compressed optical pulse.

The SMF used in the experiment is HI1060. The total GVD inside the resonator is positive, with a value of 0.0434 ps^2 corresponding to the center wavelength of 1.03 μm. Therefore, the laser operates in the normal dispersion region of the 1.0 μm wavelength band. A non-zero GVD value contains frequency components in a wide range when the pulse travels through the optical fiber, resulting in chirping. To compensate for this, pulses output directly from the laser require compression.

The bottom box in Fig. 1 depicts the experimental setup for pulse compression. A reflective diffraction grating with 600 grooves/mm and exhibiting polarization-dependence is used. Consequently, the HWP is inserted into the path of the light pulse output directly from the PBS. After passing through the HWP, the light enters the first diffraction grating. Subsequently, the diffracted light enters the second diffraction grating. The diffracted light proceeds parallelly, and its height is adjusted by inserting a mirror into its path. The pulse is compressed when the reflected light passes through a pair of gratings in the opposite direction to that of the incident light.

The optical spectrum of the optical pulse generated by the mode locked YDF laser is depicted in Fig. 2(a). The center wavelength and the full width at half maximum (FWHM) are observed to be 1035.0 nm and 17.0 nm, respectively. The inset in the Fig. 2(a) depicts the optical spectrum on a dB scale. We observe side peaks at both ends of the optical spectrum, revealing a typical dissipative soliton oscillating in the normal dispersion region of the mode-locked fiber laser. The RF-spectrum output of the mode-locked YDF laser with a side mode suppression ratio of approximately 53.44 dB and a repetition rate of 103.75 MHz is depicted in Fig. 2(b). The threshold pump output of the mode-locked fiber laser is 350 mW, above which pulses are generated by self-starting. The output power is observed to be approximately 67 mW corresponding to an optical pump power of 350 mW. This indicates that the output pulse obtained directly from the laser contains multiple frequency components and is highly chirped. The duration of the output pulse emitted by the laser is measured using an interferometric autocorrelation. The measured optical pulse width is ~ 3.4 ps under the assumption of a Gaussian profile, as recorded in Fig. 3(a). The time bandwidth product of the optical pulse is observed to be 16.2, which is significantly larger than the transform limited value of 0.44 for pulses of Gaussian shape. This can be attributed to the highly chirped nature of the pulse. The autocorrelation trace of the compressed optical pulse following its passage through the pulse compression system is depicted in Fig. 3(b). It showed several side-lobes, which arise from the steep sides and structure of the spectrum [30]. The compressed pulse width is observed to be 172 fs, assuming the pulse shape to be Gaussian, and the average output power exceeds ~40 mW. The time bandwidth product of the compressed pulse is reduced to 0.82. This is significantly different from the transform-limited value owing to the lack of higher-order compensation during dispersion compensation using the diffraction grating.

A schematic diagram of the experimental setup for a PCA-based THz-TDS using a mode-locked YDF laser is depicted in Fig. 4. Initially, compressed optical pulses are incident on THz-TDS. They are split into beams of approximately equal intensity using a beam splitter and the two beams are incident on the emitter (Tx) and the receiver (Rx). A corner-cube retroreflector is affixed to the variable stage connected by a motor, enabling the adjustment of the time delay in the optical path by moving it into the optical path of Tx. Tx is taken to be a dipole antenna with a gap of 5 μm and a width of 10 μm. In contrast, Rx is taken to be a

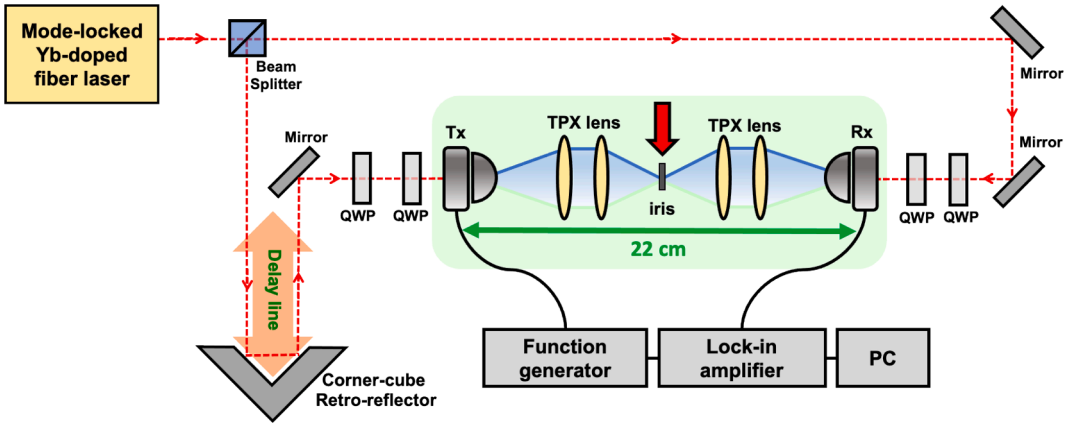

Fig. 4. Schematic diagram of the experimental setup for THz TDS (QWP: Quarter wave-plate, Tx: THz emitter, Rx: THz receiver).

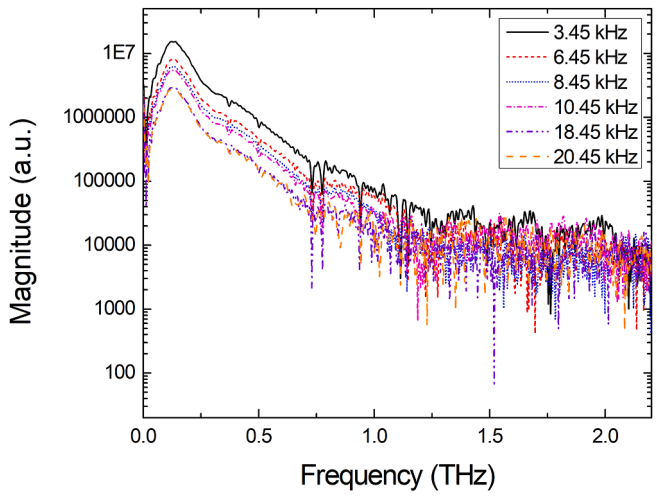

Fig. 5. Variations of the THz spectra of the 220 mm free space with respect to the bias frequency of Tx.

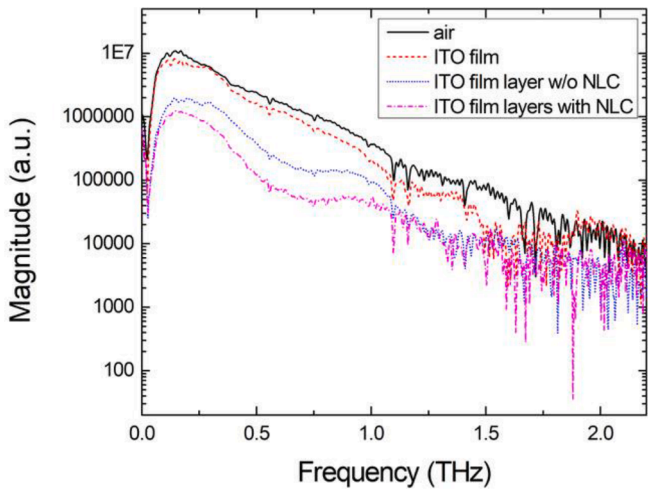

Fig. 7. THz Transmission spectra of the NLC cell with ITO electrodes under various conditions.

bow-tie antenna with an antenna gap of 5 μm and a width of 10 μm. Both antennas are commercially obtained from Batop, and exhibit 84% light absorption and 300 fs carrier recovery time in the 1060 nm wavelength band. Each QWP is inserted in front of the antenna such that it is incident with linearly polarized light. The free space between the two antennas is taken to be 220 mm, and the signal is detected using a lock-in amplifier. The radiated THz waves are aligned using a silicon lens placed in front of each antenna and two pairs of TPX lenses. The refractive index of the TPX lenses used in the experiment is 1.45 (@1 THz), and the focal length is 32.5 mm. The average optical power of the optical pulse beam incident on each antenna is set to be 20 mW, and the peak power and pulse energy of the pulse are 1.12 kW and 192 pJ, respectively. The sensitivity and signal-to-noise ratio (SNR) of the THz radiation signal are observed to be dependent on various parameters, such as bias voltage, frequency, and humidity within the free space. The THz spectrum of the 220 mm free space is measured by varying the frequency of the bias voltage connected to Tx from 3.45 kHz to 20.45 kHz. As depicted in Fig. 5, the sensitivity of the signal is observed to be inversely proportional to the frequency, but the SNR does not exhibit significant dependence on the latter. However, as the bias frequency is increased, the THz bandwidth is observed to decrease. In the region above 20.45 kHz, the water vapor peak after 0.75 THz is similar to the noise level, making it difficult to distinguish the signal. Under all measurement conditions, the humidity and the bias frequency are set to approximately 40–45%, and 4.25 kHz, respectively. For the free space of 220 mm, an SNR of approximately 40 dB is obtained, and the frequency bandwidth of the THz wave is confirmed to be 2.2 THz or higher.

Next, an E7 NLC cell is fabricated and the dependence of its THz absorption spectrum on the applied electric field is measured and analyzed using THz-TDS. The E7 NLC used in the experiment is a mixture of 5CB, 7CB, 8OCB, and 5CT of cyanide-added polyphenyl substances in the specific compositional ratio of 51%, 25%, 16%, and 8%, respectively [52]. Z-cut quartz wafers are commonly used as a substrate during THz spectroscopy to avoid birefringence due to their effect on light waves propagating perpendicular to the wafer surface [53]. In our first attempt, an NLC cell is fabricated using z-quartz, which is known to exhibit excellent THz wave transmission properties. However, during the coating of the electrode metal on the z-quartz, a large absorption is observed in the THz band, complicating the measurement of the spectral characteristics of the NLC cell in the THz band. Therefore, during the second attempt, the substrate of the LC cell is fabricated by replacing z-quartz with an indium tin oxide (ITO) coated Polyethylene Terephthalate (PET) film [54]. A schematic diagram of an NLC cell fabricated using a 0.1 mm thick ITO film as an electrode and a substrate is depicted in Fig. 6(a). A polyimide layer is subsequently applied to the film, cured, and aligned to align the LC molecules in the direction parallel to the ITO film. As illustrated in Fig. 6(b), the thickness of the NLC layer is 30 μm, and the total thickness of the cell including the ITO substrate is 230 μm. The wires are connected by soldering indium to the electrodes.

The THz transmission spectra of the NLC cell fabricated with an ITO film as an electrode are depicted in Fig. 7. A comparison of the THz spectrum in free space with that obtained when a single ITO film is utilized in the absence of LC molecules reveals that the signal sensitivity decreases slightly until the 1.5 THz region approximately. However, the sensitivity of the THz spectrum decreases by approximately 10 dB

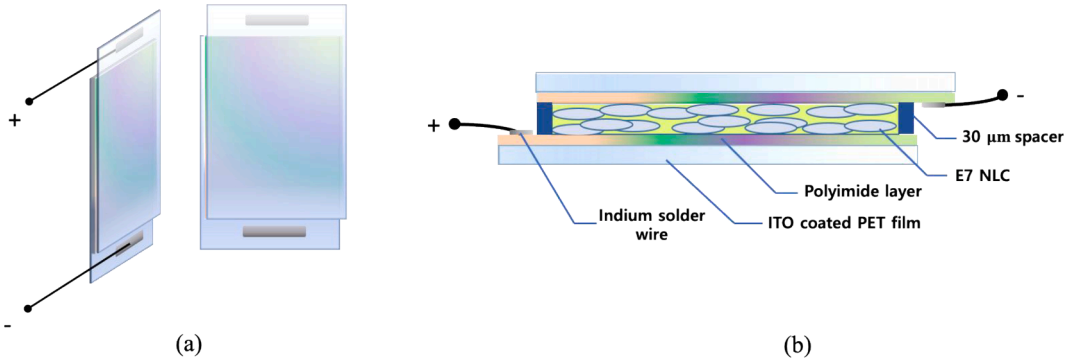

Fig. 6. (a) A schematic diagram of the LC cell with an ITO film and (b) the structure of the NLC cell with ITO electrodes and substrates.

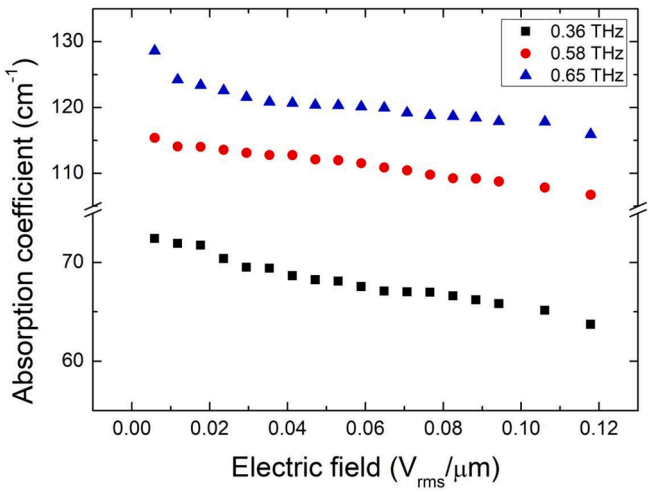

Fig. 8. Variations of absorption coefficient at a specific THz frequency with respect to the electric field applied to the NLC cell.

irrespective of the presence of LC molecules in the cell substrate constructed using an ITO film. Beyond 1.5 THz, it becomes difficult to distinguish due to its similarity with the noise signal.

As indicated in the experimental setup depicted in Fig. 4, the focal point of the THz wave is in the middle area of the free space, and an aperture is placed in this area. The radius of the aperture is set to approximately 8 mm, minimizing the loss of the THz wave the focal position, and the NLC cell is positioned directly behind the aperture to block the signal reflected from the surface of the NLC cell. Therefore, the THz wave passes solely through the NLC cell. The THz absorption spectra of the NLC cell are measured by applying an electric field to it. The direction of the applied electric field is aligned perpendicular with the director of the LC. The THz absorption coefficient with respect to the intensity of the applied electric fields to the NLC cell is depicted in Fig. 8. The intensity of the electric field is varied from 0.005 V_{rms}/μm to 0.12 V_{rms}/μm. The THz absorption coefficient is observed to decrease as the intensity of the electric field is increased. This can be attributed to the change in the effective refractive index of the NLC and the decrease in the transmitted signal of the linearly polarized THz wave with rotation of the LC director.

3. Summary

In this paper, PCA-based terahertz time-domain spectroscopy (THz-TDS) was fabricated using a mode-locked ytterbium fiber laser as a pump light source. The THz-TDS exhibited a spectrum exceeding 2.2 THz over a free space of 220 mm. Subsequently, an E7 nematic liquid crystal (NLC) cell was fabricated to apply the THz-TDS, and the THz absorption spectrum corresponding to an external signal applied to the NLC cell was measured. An NLC cell was fabricated using an ITO film as the substrate and the electrode. As the electric field applied to the NLC cell was increased, the director of the LC was observed to be aligned in the direction of the electric field, and the effective refractive index was observed to vary correspondingly. In turn, the THz absorption spectrum was observed to decrease.

Author statement

Hansol Choi and Jisu Kim carried out all experiments. They are acquisition, analysis, and interpretation of data. They contributed to writing of original draft preparation.

Soyeon Ahn prepared the sample of the namatic liquid crystal cell.

Sang Pil Han is participation in the concept of the experiments.

Zhongping Chen and Min Yong Jeon are supervised.

Min Yong Jeon contributed to writing and review and editing.

All authors have read and agreed to the published version of the manuscript.

Declaration of Competing Interest

The authors declare that they have no known competing financial interests or personal relationships that could have appeared to influence the work reported in this paper.

Acknowledgments

This research was supported by Chungnam National University of Korea and was supported by Basic Science Research Program through the National Research Foundation of Korea (NRF) funded by the Ministry of Science, ICT and future Planning (NRF-2019R1A2C1084933, NRF-2020R1A6A1A03047771) and was supported by a Korea Institute for Advancement of Technology (KIAT) grant funded by the Korea Government (MOTIE) (P0008458, The Competency Development Program for Industry Specialist).

References

[1] M. Tonouchi, Cutting-edge terahertz technology, Nat. Photonics 1 (2007) 97–105.
[2] K. Kawase, Y. Ogawa, Y. Watanabe, H. Inoue, Non-destructive terahertz imaging of illicit drugs using spectral fingerprints, Opt. Express 11 (2003) 2549–2554.
[3] T. Yasui, T. Yasuda, K.-I. Sawanaka, T. Araki, Terahertz paintmeter for noncontact monitoring of thickness and drying progress in paint film, Appl. Opt. 44 (2005) 6849–6856.
[4] J.-Y. Lu, L.-J. Chen, T.-F. Kao, H.-H. Chang, H.-W. Chen, A.-S. Liu, Y.-C. Chen, R.-B. Wu, W.-S. Liu, J.-I. Chyi, C.-K. Sun, Terahertz microchip for illicit drug detection, IEEE Photon. Technol. Lett. 18 (2006) 2254–2256.
[5] H. Guerboukha, K. Nallappan, M. Skorobogatiy, Toward real-time terahertz imaging, Adv. Opt. Photonics 10 (2018) 843–938.
[6] L. Yu, L. Hao, T. Meiqiong, H. Jiaoqi, L. Wei, D. Jinying, C. Xueping, F. Weiling, Z. Yang, The medical application of terahertz technology in non-invasive detection of cells and tissues: opportunities and challenges, RSC Adv. 9 (2019) 9354–9363.
[7] M. Manjappa, R. Singh, Materials for terahertz optical science and technology, Adv. Opt. Mater. 8 (2020) 1901984.
[8] G. Musina, P. Nikitin, N. Chernomyrdin, I. Dolganova, A. Gavdush, G. Komandin, D. Ponomarev, A. Potapov, I. Reshetov, V. Tuchin, K. Zaytsev, Prospects of terahertz technology in diagnosis of human brain tumors – a review, J. Biomed. Photonics Eng. 6 (2020), 020201.
[9] Y. Tao, A. Fitzgerald, V. Wallace, Non-contact, non-destructive testing in various industrial sectors with terahertz technology, Sensors 20 (2020) 712.
[10] M. Kato, S.R. Tripathi, K. Murate, K. Imayama, K. Kawase, Non-destructive drug inspection in covering materials using a terahertz spectral imaging system with injection-seeded terahertz parametric generation and detection, Opt. Express 24 (2016) 6425–6432.
[11] F. D'Angelo, Z. Mics, M. Bonn, D. Turchinovich, Ultra-broadband THz time-domain spectroscopy of common polymers using THz air photonics, Opt. Express 22 (2014) 12475–12485.
[12] M. Zalkovskij, C.Z. Bisgaard, A. Novitsky, R. Malureanu, D. Savastru, A. Popescu, P. U. Jepsen, A.V. Lavrinenko, Ultrabroadband terahertz spectroscopy of chalcogenide glasses, Appl. Phys. Lett. 100 (2012), 031901.
[13] J. Takayanagi, H. Jinno, S. Ichino, K. Suizu, M. Yamashita, T. Ouchi, S. Kasai, H. Ohtake, H. Uchida, N. Nishizawa, K. Kawase, High-resolution time-of-flight terahertz tomography using a femtosecond fiber laser, Opt. Express 17 (2009) 7533–7539.
[14] J.S. Kim, H.M. Yang, S.-P. Han, K. Moon, K.H. Park, M.Y. Jeon, Compact THz time-domain spectroscopy based on pre-chirped pulses from mode-locked Yb-doped fiber laser, Opt. Fiber Technol. 45 (2018) 182–187.
[15] M.S. Kong, J.S. Kim, S.P. Han, N. Kim, K. Moon, K.H. Park, M.Y. Jeon, Terahertz radiation using log-spiral-based low-temperature-grown InGaAs photoconductive antenna pumped by mode-locked Yb-doped fiber laser, Opt. Express 24 (2016) 7037–7045.
[16] T. Nagatsuma, H. Nishii, T. Ikeo, Terahertz imaging based on optical coherence tomography [Invited], Photon. Res. 2 (2014) B64–B69.
[17] K. Ahi, S. Shahbazmohamadi, N. Asadizanjani, Quality control and authentication of packaged integrated circuits using enhanced-spatial-resolution terahertz time-domain spectroscopy and imaging, Opt. Lasers Eng. 104 (2018) 274–284.
[18] M. Hassan, R.E. Abou Zeid, W.S. Abou-Elseoud, E. Hassan, L. Berglund, K. Oksman, Effect of unbleached rice straw cellulose nanofibers on the properties of polysulfone membranes, Polymers 11 (2019) 938.
[19] L. Zanotto, R. Piccoli, J. Dong, D. Caraffini, R. Morandotti, L. Razzari, Time-domain terahertz compressive imaging, Opt. Express 28 (2020) 3795–3802.
[20] J. Federici, L. Moeller, Review of terahertz and subterahertz wireless communications, J. Appl. Phys. 107 (2010) 6.

[21] H. Shams, M.J. Fice, K. Balakier, C.C. Renaud, F. van Dijk, A.J. Seeds, Photonic generation for multichannel THz wireless communication, Opt. Express 22 (2014) 23465–23472.
[22] H. Elayan, O. Amin, R.M. Shubair, M. Alouini, Terahertz communication: The opportunities of wireless technology beyond 5G, in: 2018 International Conference on Advanced Communication Technologies and Networking (CommNet), 2018, pp. 1–5.
[23] S.-P. Han, N. Kim, H. Ko, H.-C. Ryu, J.-W. Park, Y.-J. Yoon, J.-H. Shin, Compact fiber-pigtailed InGaAs photoconductive antenna module for terahertz-wave generation and detection, Opt. Express 20 (2012) 18432–18439.
[24] N. Kim, J. Shin, E. Sim, C.W. Lee, D.-S. Yee, M.Y. Jeon, Y. Jang, K.H. Park, Monolithic dual-mode distributed feedback semiconductor laser for tunable continuous-wave terahertz generation, Opt. Express 17 (2009) 13851–13859.
[25] M.Y. Jeon, N. Kim, J. Shin, J.S. Jeong, S.-P. Han, C.W. Lee, Y.A. Leem, D.-S. Yee, H. S. Chun, K.H. Park, Widely tunable dual-wavelength E^{r3}+-doped fiber laser for tunable continuous-wave terahertz radiation, Opt. Express 18 (2010) 12291–12297.
[26] G. Chang, C.J. Divin, J. Yang, M.A. Musheinish, S.L. Williamson, A. Galvanauskas, T.B. Norris, GaP waveguide emitters for high power broadband THz generation pumped by Yb-doped fiber lasers, Opt. Express 15 (2007) 16308–16315.
[27] R.J.B. Dietz, R. Wilk, B. Globisch, H. Roehle, D. Stanze, S. Ullrich, S. Schumann, N. Born, M. Koch, B. Sartorius, M. Schell, Low temperature grown Be-doped InGaAs/InAlAs photoconductive antennas excited at 1030 nm, J. Infrared Millimeter Waves 34 (2013) 231–237.
[28] A. Brahm, A. Wilms, R.J. B. Dietz, T. Göbel, M. Schell, G. Notni, A. Tünnermann, Multichannel terahertz time-domain spectroscopy system at 1030 nm excitation wavelength, Opt. Express 22 (2014) 12982-12993.
[29] J.S. Kim, H.M. Yang, M.S. Kong, M.Y. Jeon, Characterization of normal dispersion mode-locked Yb-doped fiber laser with birefringent spectral filter, Opt. Eng. 57 (2017), 021204.
[30] A. Chong, J. Buckley, W. Renninger, F. Wise, All-normal-dispersion femtosecond fiber laser, Opt. Express 14 (2006) 10095–10100.
[31] P. Qin, Y. Song, H. Kim, J. Shin, D. Kwon, M. Hu, C. Wang, J. Kim, Reduction of timing jitter and intensity noise in normal-dispersion passively mode-locked fiber lasers by narrow band-pass filtering, Opt. Express 22 (2014) 28276–28283.
[32] M. Suzuki, R.A. Ganeev, S. Yoneya, H. Kuroda, Generation of broadband noise-like pulse from Yb-doped fiber laser ring cavity, Opt. Lett. 40 (2015) 804–807.
[33] Z. Luo, Y. Huang, J. Wang, H. Cheng, Z. Cai, C. Ye, Multiwavelength dissipative-soliton generation in Yb-fiber laser using graphene-deposited fiber-taper, IEEE Photon. Technol. Lett. 24 (2012) 1539–1542.
[34] K. Niu, R. Sun, Q. Chen, B. Man, H. Zhang, Passively mode-locked Er-doped fiber laser based on SnS2 nanosheets as a saturable absorber, Photonics Res. 6 (2018) 72–76.
[35] N. Xu, P. Ma, S. Fu, X. Shang, S. Jiang, S. Wang, D. Li, and H. Zhang, Tellurene-based saturable absorber to demonstrate large-energy dissipative soliton and noise-like pulse generations, Nanophotonics, 9 (2020) 2783-2795.
[36] X. Shang, L. Guo, H. Zhang, D. Li, Q. Yue, Titanium disulfide based saturable absorber for generating passively mode-locked and Q-switched ultra-fast fiber lasers, Nanomaterials 10 (2020) 1922.
[37] A.F.J. Runge, C. Aguergaray, R. Provo, M. Erkintalo, N.G.R. Broderick, All-normal dispersion fiber lasers mode-locked with a nonlinear amplifying loop mirror, Opt. Fiber Tech. 20 (2014) 657–665.
[38] K. Özgören, F.Ö. Ilday, All-fiber all-normal dispersion laser with a fiber-based Lyot filter, Opt. Lett. 35 (2010) 1296–1298.
[39] N. Ming, S. Tao, W. Yang, Q. Chen, R. Sun, C. Wang, S. Wang, B. Man, H. Zhang, Mode-locked Er-doped fiber laser based on PbS/CdS core/shell quantum dots as saturable absorber, Opt. Express 26 (2018) 9017–9026.
[40] K.-H. Kim, D.H. Song, Z.-G. Shen, B.W. Park, K.-H. Park, J.-H. Lee, T.-H. Yoon, Fast switching of long-pitch cholesteric liquid crystal device, Opt. Express 19 (2011) 10174–10179.
[41] M.O. Ko, S.-J. Kim, J.-H. Kim, B.W. Lee, M.Y. Jeon, Dynamic measurement for electric field sensor based on wavelength-swept laser, Opt. Express 22 (2014) 16139–16147.
[42] M.O. Ko, S.-J. Kim, J.-H. Kim, M.Y. Jeon, In situ observation of dynamic pitch jumps of in-planar cholesteric liquid crystal layers based on wavelength-swept laser, Opt. Express 26 (2018) 28751–28762.
[43] R. Ozaki, K. Kihara, K. Matsuura, K. Kadowaki, T.Q. Duong, H. Moritake, Wavelength and bandwidth control of stop band of ferroelctric liquid crystals by varying incident angle and electric field, Appl. Phys. Express 13 (2020), 051003.
[44] S. Ahn, M.O. Ko, J.-H. Kim, Z. Chen, M.Y. Jeon, Characterization of second-order reflection bands from a cholesteric liquid crystal cell based on a wavelength-swept laser, Sensors 20 (2020) 4643.
[45] N. Vieweg, B.M. Fischer, M. Reuter, P. Kula, R. Dabrowski, M.A. Celik, G. Frenking, M. Koch, P.U. Jepsen, Ultrabroadband terahertz spectroscopy of a liquid crystal, Opt. Express 20 (2012) 28249–28256.
[46] Xuefeng Li, Nicholas Tan, Mike Pivnenko, Juraj Sibik, J. Axel Zeitler and Daping Chu, High-birefringence nematic liquid crystal for broadband THz applications, Liquid Crystals 43 (2016) 955-962.
[47] C.-S. Yang, C. Kuo, P.-H. Chen, W.-T. Wu, R.-P. Pan, P. Yu, and C.-L, Pan, High-transmittance 2π electrically tunable terahertz phase shifter with CMOS-compatible driving voltage enabled by liquid crystals, Appl. Sci. 9 (2019) 271.
[48] M. Zou, S. Miyong, Y. Hua, Ultra-broadband and wide-angle terahertz polarization converter based on symmetrical anchor-shaped metamaterial, Optical Mater. 107 (2020), 110062.
[49] N. Vieweg, M.A. Celik, S. Zakel, V. Gupta, G. Frenking, M. Koch, Terahertz absorption of nematic liquid crystals, J. Infrared Milli. Terahz. Waves 35 (2014) 478–485.
[50] C.-Y. Chen, C.-L. Pan, Liquid-crystal-based terahertz tunable Lyot filter, Appl. Phys. Lett. 88 (2006), 101107.
[51] R. Zheng, E.H.W. Chan, X. Wang, Microwave photonic devices based on liquid crystal on silicon technology, Appl. Sci. 9 (2019) 260.
[52] A. Jafari, A. Ghanadzadeh, H. Tajalli, M. Yeganeh, M. Moghadam, Electronic absorption spectra of cresyl violet acetate in anisotropic and isotropic solvents, Spectrochimica Acta A 66 (2007) 717–725.
[53] C.L. Davies, J.B. Patel, C.Q. Xia, L.M. Herz, M.B. Johnston, Temperature-dependent refractive index of quartz at terahertz frequencies, J Infrared Milli Terahz waves 39 (2018) 1236–1248.
[54] C.-S. Yang, C.-M. Chang, P.-H. Chen, P. Yu, C.-L. Pan, Broadband terahertz conductivity and optical transmission of indium-tin-oxide (ITO) nanomaterials, Opt. Express 21 (2013) 16670–16682.